NANO · MICRO small
www.small-journal.com

Coaxial Flexible Fiber-Shaped Triboelectric Nanogenerator Assisted by Deep Learning for Self-Powered Vibration Monitoring

Cong Zhao, Taili Du, Bin Ge, Ziyue Xi, Zian Qian, Yawei Wang, Junpeng Wang, Fangyang Dong, Dianlong Shen, Zhenhao Zhan, and Minyi Xu**

Self-powered vibration sensor is highly desired for distributed and continuous monitoring requirements of Industry 4.0. Herein, a flexible fiber-shaped triboelectric nanogenerator (F-TENG) with a coaxial core-shell structure is proposed for the vibration monitoring. The F-TENG exhibits higher adaptability to the complex surfaces, which has an outstanding application prospect due to vital compensation for the existing rigid sensors. Initially, the contact characteristics between the dielectric layers, that related to the perceiving performance of the TENG, are theoretically analyzed. Such a TENG with 1D structure endows high sensitivity, allowing for accurately responding to a wide range of vibration frequencies (0.1 to 100 Hz). Even applying to the real diesel engine, the error in detecting the vibration frequencies is only 0.32% compared with the commercial vibration sensor, highlighting its potential in practical application. Further, assisted by deep learning, the recognition accuracy in monitoring nine operating conditions of the system achieves 97.87%. Overall, the newly designed F-TENG with the merits of high-adaptability, cost-efficiency, and self-powered, has offered a promising solution to fulfill an extensive range of vibration sensing applications in the future.

1. Introduction

In achieving the goal of the Industry 4.0, predictive maintenance holds a pivotal role, where the monitoring of appliance operating status is an essential requirement.[1–4] Vibration sensors have extensive applications in various fields including structure health monitoring, fault diagnosis, and transport safety, which are vital for reducing failure rates and enhancing security.[5–7] However, the existing vibration sensing technologies still face certain challenges during the actual promotion process. For instance, commercial vibration sensors (e.g., accelerometers) heavily rely on cable-based power supply.[8,9] Cable-based power supply entails challenges for in situ vibration monitoring such as complex layout arrangements and increased expenses of installation.[10] Although the vibration sensors based on optical fibers have been proposed, their operation still requires continuous input of the optical signals.[11–13] Considering these, the self-powered sensors have provided a promising outlook for overcoming the reliance on the cables.[14–16] Despite significant progress in the advancement of piezoelectric ceramics as self-powered sensors, they still confront the drawbacks related to weak output and complicated fabrication process.[17–19] And, piezoelectric sensors are susceptible to fatigue failure and depolarization as subjected to prolonged vibration.[20,21] Last but not least, their feature of rigidity inevitably presents the problems of layout as placing on the curved surfaces, necessitating modifications to the attachment surfaces.[22,23] Therefore, it has been an urgent requirement for developing self-powered yet adaptive vibration sensing technology for the demand of comprehensive vibration monitoring in Industry 4.0.

Recently, triboelectric nanogenerators (TENGs) have garnered increasing research interest for their applications as self-powered sensors across diverse domains owing to the merits of widespread availability, easy manufacturability and high flexibility.[24–28] Researchers have also made endeavors toward developing various types of TENG-based vibration sensors. To date, the majority of vibration sensors based on TENG have been constructed with rigid parts such as the bouncing ball, sliding block, cantilever,[10,29–31] which faces the same issue with piezoelectric sensors. To address the issue above, recent considerable progress proposed a fully soft vibration sensor based on liquid metal droplet and patterned laser-induced graphene surface

C. Zhao, T. Du, B. Ge, Z. Xi, Z. Qian, Y. Wang, J. Wang, F. Dong, D. Shen, Z. Zhan, M. Xu
Dalian Key Laboratory of Marine Micro/Nano Energy and Self-powered Systems
Marine Engineering College
Dalian Maritime University
Dalian 116026, China
E-mail: dutaili@dlmu.edu.cn; xuminyi@dlmu.edu.cn
T. Du
Collaborative Innovation Research Institute of Autonomous Ship
Dalian Maritime University
Dalian 116026, China
B. Ge
The Sixth Institute
601 Branch of China Aeronautical Science and Technology Corporation
Hohhot 010076, China
The ORCID identification number(s) for the author(s) of this article can be found under https://doi.org/10.1002/smll.202307680

DOI: 10.1002/smll.202307680

fabricated by the laser direct writing method. While the liquid electrodes face the potential risk of leakage, especially after long-term vibration.[32] Due to the same issue, a TENG utilized layer-particle-layer structure, enabling alternating contact between the particles and graphite-based membranes under vibration waves ranging from 3 to 170 KHz.[22] However, this flexible TENG is mainly designed for perceiving ultrahigh frequencies, limiting its extensive applications. Unlike the 2D planar structure above, 1D coaxial core-sheath architecture possesses the electronics with flexibility, softness, and shape adaptability.[33–37] In addition, slender structure, owing to its feature of low inherent damping, making it highly responsive to external stimuli, and facilitates easy contact between triboelectric layers.[38,39]

Herein, this work proposed a fiber-shaped triboelectric nanogenerator (namely, the F-TENG) for vibration monitoring. The flexible device has possessed extraordinary adaptability, allowing the device to overcome the constrains imposed by curved attachment surfaces without requiring additional modification. The detection mechanism is clarified through the proposed dynamics model in this work. Furtherly, the F-TENG is optimized through considering factors including the diameters, materials, and stretching ratio. Based on the experimental results, it can detect a broad frequency range between 0.1 and 100 Hz. Even applying in the real diesel engine, the error in sensing vibration frequencies is only 0.32%. Finally, a pipe condition monitoring is constructed and the voltage outputs of the F-TENG are collected under 9 typical conditions and further trained by deep learning. With an accuracy of 97.87%, the F-TENG can recognize working conditions and intelligently diagnose faults.

2. Structure Design and Fabrication of the F-TENG

Figure 1a depicts the core-shell coaxial structure of the device, comprising a silicone-based core and outer tube. Figure 1b illustrates the preparation of silicone elastomer (Dragon skin 00–30) by uniformly mixing equal proportions of its part A and part B components. The air bubbles, that trapped in the mixed solution, are removed by vacuuming for ≈3 min. In order to ease the subsequent demolding process, the release agent is injected into the mold. Then, we infuse the prepared solution into a glass mold (length: 20 cm, inner diameter: 3 mm). Following a curing process in a drying chamber at 40 °C for ≈5 h, the silicone-based column is removed as the substrate. Then, flexible conductive yarn, as the electrode of the F-TENG, is wrapped around the silicone substrate and clamped at one end of another PET tube (length: 20 cm, inner diameter, 4 mm). The wrapped conductive yarn is subsequently covered by the silicone rubber solution. The PET mold is peeled off as the silicone rubber is fully dried and obtain the silicone-based inner core of the F-TENG. Ultimately, the outer tube (length: 20 cm, inner diameter: 6 mm) and core are assembled together to obtain the F-TENG. All of the materials and processes are feasible for fabricating, revealing its merit of industry-friendly.

The conductive yarn, fully encapsulated into the inner core, serves as the electrode of the device due to superior conductivity (4-6 Ωcm^{-1}), formability and easy accessibility. The conductive yarns are helically embedded in the silicone elastomer, which can effectively avoid the mismatch of Young's modulus between the dielectric layer and electrode. As depicted in Figure 1c-i, the conductive yarn is observed through the field emission scanning electron microscopy (FESEM). The conductive yarn is fabricated by twisting several bright wires (diameter, ≈20 μm) together (Figure 1c-ii). The conductive yarn used here are acquired through plating silver on the surface of nylon yarns. And energy dispersive spectrometer (EDS) map of the conductive yarn reveals the presence of the element Ag on the surface, which is the main contribution to the conductivity of the yarn (Figure 1c-iii).

Figure 1d schematically exhibits the perceiving mechanism of the device. The latex tube periodically contacts the inner core as exerting vibrational excitation. Latex tube and silicone rubber surface are charged positively and negatively due to their electronegativity difference. Initially, the outer tube and core stay at their original position (Figure 1d-i). The upward vibration causes the deformation of the device, disrupting the electrostatic equilibrium. Consequently, the electrons flow from ground to conductive yarn (Figure 1d-ii). Then, a new equilibrium state is established at the point of maximum displacement, and the amount of the transferred charges reaches maximum value (Figure 1d-iii). Finally, the electrons flow from conductive yarn to ground at the separation process during the down movement (Figure 1d-iv). Through the COMSOL Multiphysics, the electric potential distribution between the silicone-based core and latex tube is simulated to verify the present working mechanism (Figure 1e).

3. Results and Discussion

3.1. Optimization of the F-TENG

To analyze the mechanical characteristics of the F-TENG, a theoretical model under vibration excitation is established as shown in **Figure 2**a. Initially, it is assumed that the linear density (ρ) of the F-TENG is constant, and the internal tension between each section of F-TENG is equal to the tensile force (T). Cable element with length of Δx is taken at a distance of x from the zero point. Under the exciting force of $F(x,\ t)$, $u(x,\ t)$ refers to the cable element deflection at time t. Based on Newton's second law, the formula is as follows:

$$\frac{\rho \Delta x \partial^2 u(x,t)}{\partial t^2} = T_2 \sin\beta + F(x,t) - T_1 \sin\alpha - \rho \Delta x g \tag{1}$$

where g refers to the gravitational acceleration. T_1, T_2 are the tensile force acting on two ends of the cable element, respectively. α, β are angles between T_1, T_2 and horizontal direction. The formula of the cable element in horizontal direction can be written as:

$$T_1 cos\alpha = T_2 cos\beta = T \tag{2}$$

By solving the Equations (1) and (2) together, the deflection of the F-TENG at any given point, subjected to the external force $F(x,\ t)$, can be determined, which is:

$$\frac{\partial^2 u(x,t)}{\partial t^2} = \frac{T}{\rho}\left(\frac{\partial^2 u(x,t)}{\partial x^2}\right) - g + f(x,t) \tag{3}$$

where $f(x,\ t)$ is the exciting force per unit mass at time t. It is found that tensile force, linear density of the device, and exciting

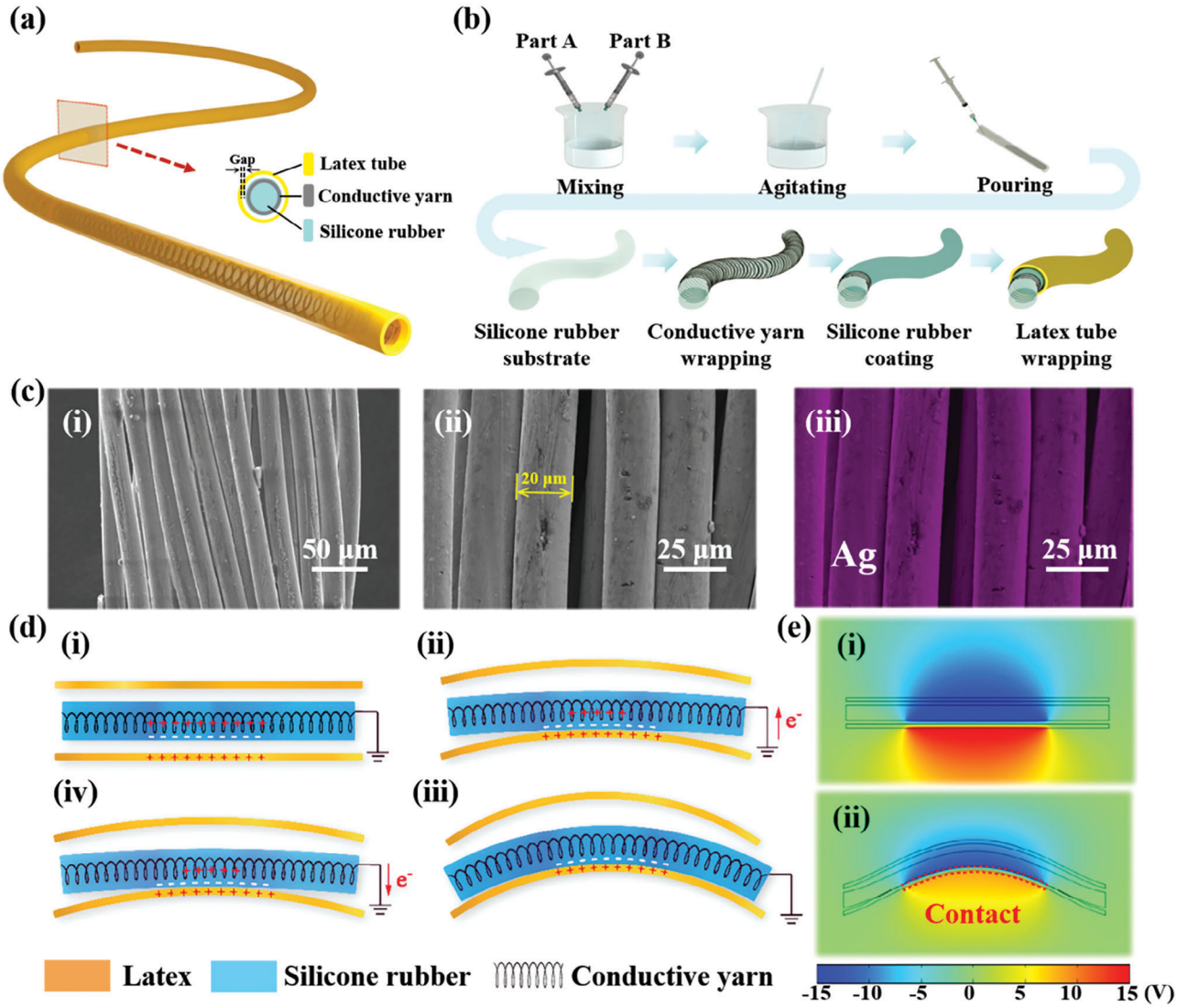

Figure 1. Structural design and perceiving mechanism of the device. a) Structure schematic of the F-TENG, and the inset showing the cross-sectional view of the device. b) Schematic illustration depicting the fabrication procedure of the device. c-i,ii) FESEM of the conductive yarn at various magnification. iii) EDS mapping of the conductive yarn. d) Schematic depiction of the perceiving mechanism. e) Electrical potential distributions of the F-TENG through COMSOL software.

force are main factors that affects the vibration characteristic of the device, and radial deflection varies with the positions of F-TENG.

In accordance with the theoretical analysis, the mechanical behavior under the external load is simulated through a finite element analysis. The F-TENG with two ends fixed, undergoes deformation as applying an exciting force of 0.15 N to the lower surface of latex tube (Figure 2b-i). The maximum radial displacement is observed at the central portion of the F-TENG, gradually decreasing along both sides in the axial direction. Figure 2b-ii exhibits the sectional drawing of the simulation, in which the underside of latex tube contacts with the silicone rubber core as F-TENG deforms under external stimulus. Figure 2c shows the simulation result on the geometric coordinates of outer tube and inner core under initial state and external load.

Then, deformation characteristics of the F-TENG is further simulated as the external loads vary from 0 to 0.15 N. As shown in Figure 2d, the radial displacement of center point of the F-TENG rises rapidly with the load varying from 0 to 0.02 N, and then gradually slows down. The reason can be explained that the increasing of external loads leads to the raising of the internal tension of the F-TENG, thereby restricting its radial displacement. Figure S1 (Supporting Information) exhibits the detailed simulation results of the radial displacement. And, the external load causes radial deformation of the outer tube, resulting in contact with the inner core. The contact force between them increases with the external load (Figure 2d; Figure S2, Supporting Information). Additionally, the contact area experiences rapid growth in the first step. Subsequently, the growth rate of contact area gradually diminishes, aligning with the simulation results regarding the radial displacement.

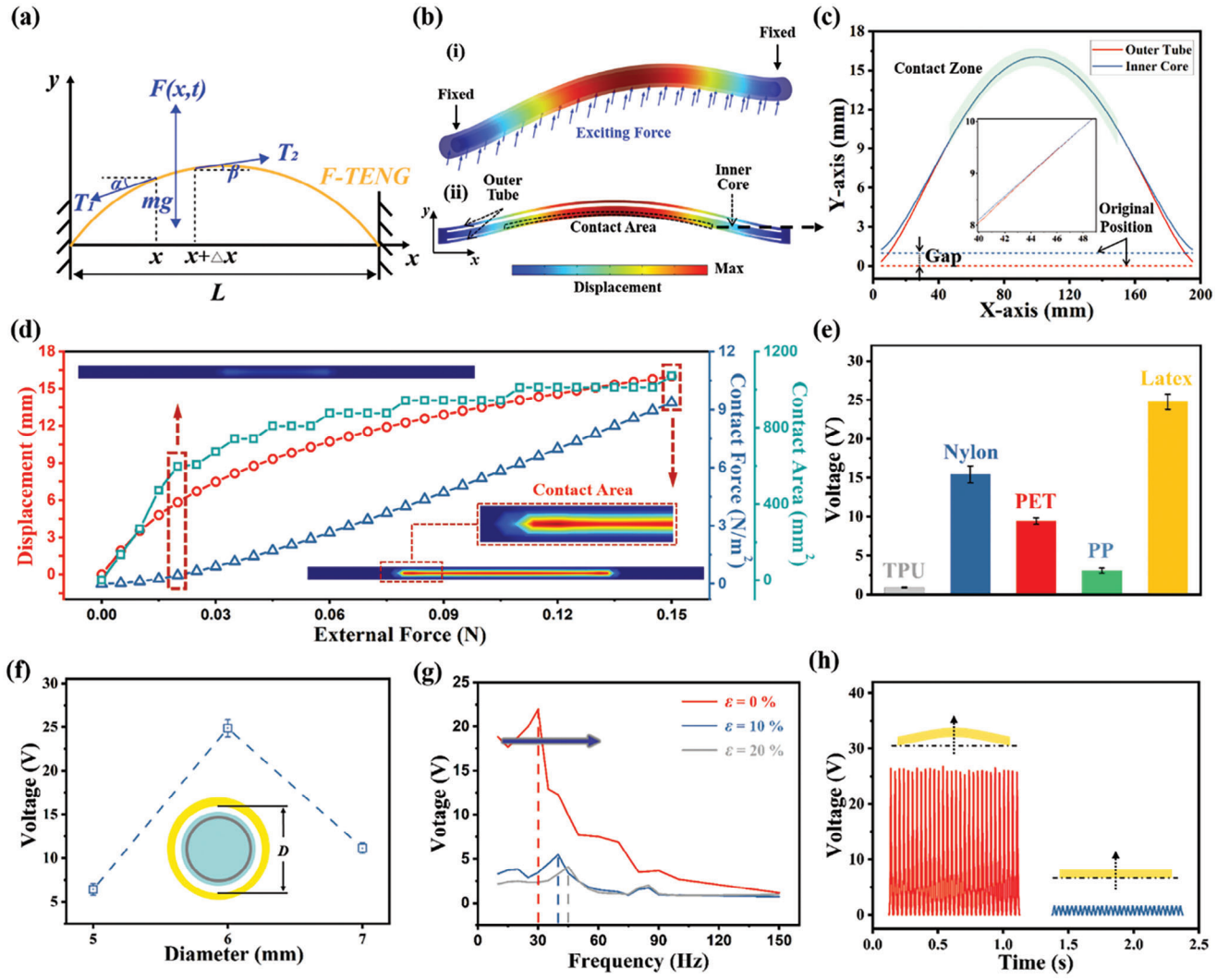

Figure 2. Mechanical characteristics analysis and optimization of F-TENG. a) Mechanical model of the device. b) Simulation of the displacement distribution for the F-TENG under the exciting forces from i) the front view and ii) the cross-section view. c) Simulated coordinates of the inner core and outer tube under the exciting forces. d) Simulated results of the displacement, contact force and contact area for the F-TENG depending on various exciting forces. e) Generated V_{oc} of the F-TENG depending on various materials of outer tube. f) Generated V_{oc} of the F-TENG depending on various inner diameters of outer tube. g) Generated V_{oc} of the F-TENG as varying λ of the inner core. h) Comparison of the V_{oc} at two various attaching methods (two-ends fixed mode, full-fixed mode).

Figure 2e displays the open-circuit voltage (V_{oc}) generated by F-TENG, which varies with the outer tube materials (e.g., thermoplastic polyurethane (TPU), nylon, polyethylene terephthalate (PET), polypropylene (PP), latex). The TENG with the latex tube produces the highest output of 25.1 V compared to those with other materials. The variation of the V_{oc} can be ascribed to two parts. One is the electronegativity difference of the materials above, and the other one is the linear density of the outer tube, which may influence the deflection of the device during the vibration process. The experimental result highlights the versatility of F-TENG in materials selection, enabling the free choice of appropriate materials for various application scenarios. In this study, high flexibility yet tough latex tube is chosen for further investigation.

Furthermore, the diameter of the silicone-based core is set at 4 mm. And the signal output generated by the device with 6 mm inner diameter latex tube is larger than those of 5 mm one (Figure 2f; Figure S3, Supporting Information). The experimental result can be explained that the larger gap between the dielectric layers results in the rising of potential difference in the process of separation.[40] Thus, the number of the electrostatic charges induced in the electrodes increases. However, the V_{oc}, short-circuit transferred charge (Q_{sc}) and short-circuit current (I_{sc}) of the F-TENG decreases to 11.1 V, 3.7 nQ, 0.4 μA with the inner diameter enlarging to 7 mm (Figure 2f; Figure S3, Supporting Information), which can be explained by the reduction in contact area between the dielectric layers.

The stretch ratio of the inner core is defined as $\lambda = L_1 - L_0/L_0$, where L_1 is the length of the inner core after stretching, L_0 is the original length. A peak voltage value of 21.9 V is observed at the frequency of 30 Hz as λ is 0% as shown in Figure 2g. However, as the stretching ratio increases to 10%, the frequency corresponding to the peak voltage (i.e., 5.5 V) shifts to 40 Hz. Similarly, at the frequency of 45 Hz, the F-TENG generates a maximum V_{oc} of 4.1 V as λ is 20%. Experimental finding indicates a substantial decline in the V_{oc} as the stretching ratio increases. It can be explained that the increase in tension limits the radial displacement of the device, thus reducing the contact area between the dielectric layers. The F-TENG exhibits resonant frequencies at 30, 40, and 45 Hz, corresponding to λ ranging from 0% to 20%. And the resonant frequency under the sinusoidal vibration can be expressed as follows:

$$f = \frac{1}{2L}\sqrt{\frac{T}{\rho}} \tag{4}$$

According to Equation (4), the resonant frequency of the F-TENG is determined by the applied tensile force, length, and density of the device. And the density of the F-TENG remains constant. Therefore, the resonant frequency of the F-TENG is mainly determined by the value of $L^{-1}T^{1/2}$. As depicted in Figure S4 (Supporting Information), the strain-tension curve of the silicone-based core reveals that values of $L^{-1}T^{1/2}$ increase with λ, subsequently leading the shift in the resonant frequency of the F-TENG. The experimental results demonstrate the convenience of adjusting the sensitivity by simply modifying the stretching ratio of the inner core, allowing for customization to meet diverse vibration monitoring requirements.

As shown in Figure 2h and Figure S5 (Supporting Information), the V_{oc}, Q_{sc}, and I_{sc} of the F-TENG is 25.8 V, 7.9 nC, 1.2 μA, respectively at the two-ends fixed mode. Interestingly, the F-TENG demonstrated its ability to function even the entire body is securely fixed on the plane of the vibration source. In this case, the latex tube remains undeformed under vibration excitation, while the flexible inner core experiences axial alternating vibrations, leading to contact-separation processes between the dielectric layers. The electrical output generated by the device under the two ends-fixed mode is larger than those of fully-secured mode (i.e., V_{oc} of 1.6 V, Q_{sc} of 0.5 nC, $I_{sc}$of 0.04 μA) as indicated in Figure 2h and Figure S5 (Supporting Information). While the frequency-domain signals of the fully-secured F-TENG still concentrate at 29.94 Hz (dominant frequency of the device) as indicated in Figure S5d (Supporting Information). The experimental results above demonstrate the advantages of the F-TENG in acquiring the frequency domain of the vibration source regardless of the arrangement methods.

3.2. Vibration Sensing Performance of the F-TENG

The vibration acceleration and frequency are the primary factors that affect the electrical outputs of the F-TENG. Herein, the F-TENG is placed on the electrodynamic shaker to evaluate the sensing performance of the device. The relationship between the vibration acceleration, frequency and amplitude under sinusoidal vibration can be expressed as:

$$y = Asin(\omega t) \tag{5}$$

$$a = A\omega^2 sin(\omega t) \tag{6}$$

where ω is the angular frequency, A is the displacement amplitude of shaker, y is the displacement.

This work investigates the output of the device under various vibration accelerations, spanning frequencies from 10 to 100 Hz. The electrical output of the F-TENG exhibits the same trend with frequencies at three different accelerations (**Figure 3**a; Figure S6, Supporting Information). The V_{oc}, Q_{sc}, and I_{sc} of the device increase with the vibration frequencies ranging from 10 to 30 Hz. However, the electrical output begins to decrease with further increase in vibration frequencies up to 100 Hz. The generated V_{oc} can reach the value of 2.2 V at the vibration acceleration of 50 m s^{-2} and frequency of 100 Hz. The signal to noise (SNR) is equal to 20lg(2.2/0.15) = 23.3 dB, where the noise is 0.15 V (inset of Figure 3a). The frequency-domain signal of the F-TENG is mainly concentrated at 100 Hz (dominant frequency) and 50 Hz (environmental interference) as shown in Figure 3b.

As depicted in Figure 3c and Figure S7 (Supporting Information), V_{oc}, Q_{sc}, and $I_{sc}$of the F-TENG increase as vibration acceleration varies from 10 to 60 m s^{-2} at the fixed frequency of 30 Hz. The increase of the V_{oc} reaveals two stages as shown in the inset of Figure 3c. In the first stage, V_{oc} of the F-TENG rises rapidly from 5.5 to 20.3 V with the vibration accelerations ranging from 10 to 40 m s^{-2}. The generated V_{oc} also rises as the vibration accelerations varies from 40 to 60 m s^{-2}. While the second stage demonstrates comparatively smaller change rate than that of the initial stage. The experimental finding aligns with the simulation trends on the contact area between the dielectric layers (Figure 2d). Diverse changes in growth rates can be explained by the changing contact area with the applied load.

Herein, the F-TENG is also demonstrated its ability in responding to the excitation with low frequencies. Initially, the F-TENG is mounted on the linear motor to investigate its working performance in responding to the movements with low frequencies. As the vibration amplitude of the linear motor rises from 5 to 100 mm, the generated V_{oc} increases from 0.1 to 0.8 V (Figure 3d). And the electrical output of the F-TENG exhibits an approximately linear increase with frequency at fixed amplitude of 100 mm (Figure 3e). At lower frequency, the internal tension force of the inner core has a longer duration to restore its original length, enabling a more effective counteraction against the deformation caused by inertia. Thereby, the radial amplitude of the inner core reduces with the frequencies. Figure 3f clearly illustrate the dependence of amplitude and frequency on the generated V_{oc}. The findings showcase the feasibility of utilizing the newly designed sensor for monitoring movement with large amplitudes at ultralow frequencies.

Moreover, the direction of vibration is a critical parameter that is related to the generated output of the device. The γ is defined as the rotating angles of the shaker (clockwise and c rotation directions are defined as positive and negative values, respectively). Figure 3g and Figure S8 (Supporting Information) exhibit the V_{oc}, Q_{sc}, and I_{sc} of the device as varying γ from −60° to 90°. The

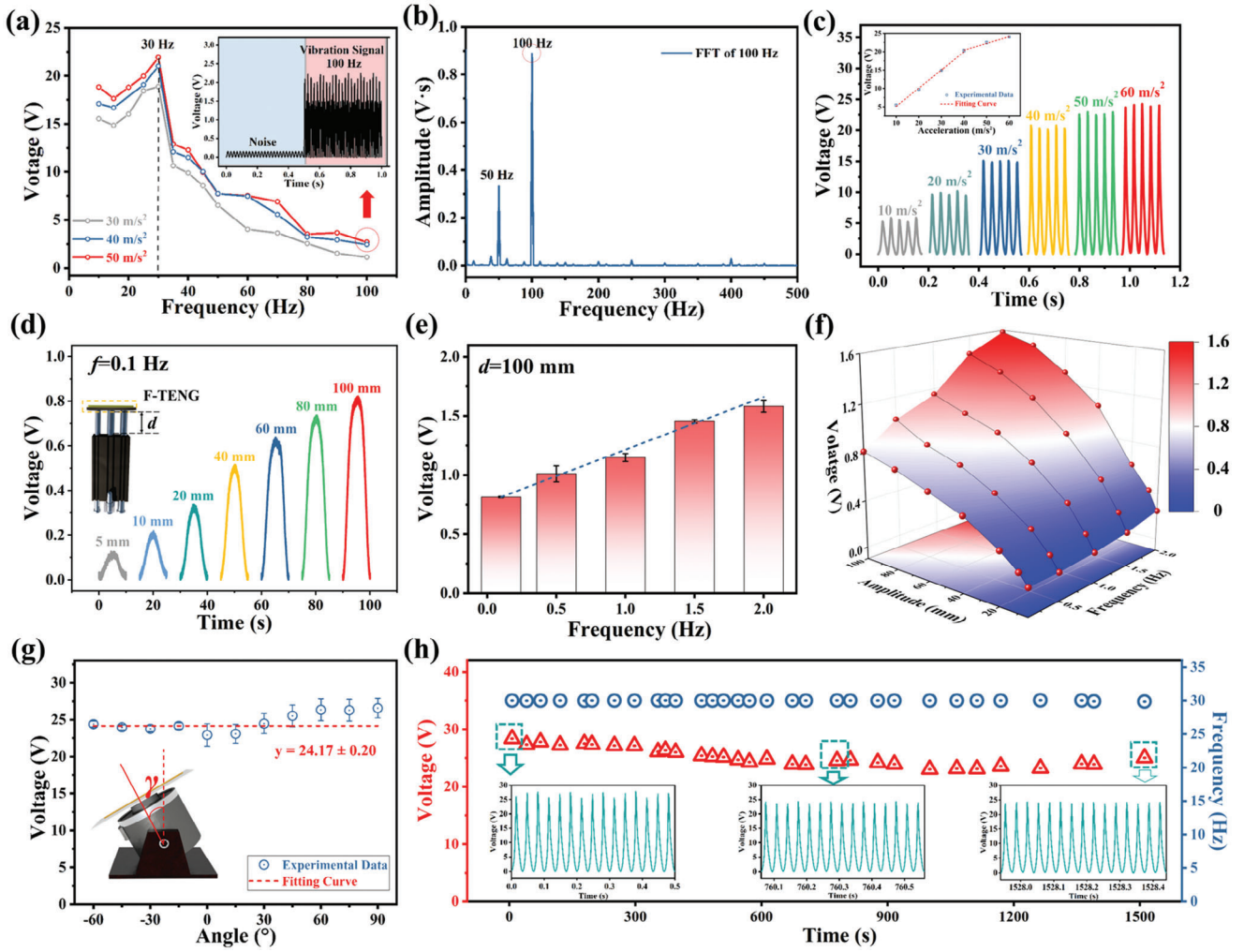

Figure 3. Vibration sensing performance of the F-TENG. a) Generated V_{oc} of the F-TENG at different vibration accelerations with frequencies ranging from 10 to 100 Hz. The inset shows the vibration signal of the device and environmental noise. b) Fourier transform of the original voltage signal of the F-TENG at the vibration frequency of 100 Hz. c) Generated V_{oc} of the F-TENG depending on various vibration accelerations at the fixed frequency of 30 Hz. d) Generated V_{oc} depending on various movement amplitude at fixed frequency of 0.1 Hz. e) Generated V_{oc} depending on various movement frequency at fixed amplitude of 100 mm. f) Relationship among the generated V_{oc} of the F-TENG, movement amplitude and frequency. g) Generated V_{oc} of the F-TENG depending on the rotating angles of the shakers. h) Durability test for the F-TENG.

direction angles have little impact on the electrical performance of the device, demonstrating its outstanding adaptability in the vibration direction. As depicted in the Figure S9 (Supporting Information), the output of the device decreases as the angle (δ) between the vibration direction and the axial line of the device increases from 0° to 90°. The reason is mainly due to the decrease in the acceleration component vertically exerted on the device (a_z) can be expressed as following:

$$a_z = a\cos\delta \tag{7}$$

According to Equation (7), theoretical output of the F-TENG should equal to zero as δ equals 0°. However, as shown in Figure S9b (Supporting Information), the generated V_{oc} of the device can still reach 1.4 V. The reason for that can be explained that the occurrence of slight vibrations in the horizontal direction leads to the contact-separation between the outer tube and core. Figure 3h shows the durability test of the device. Even after a considerable time of ≈1530 s, no evident deterioration in the electrical output is observed. And the shape of the electrical signals remain relatively constant as illustrated in the inset of Figure 3h. Additionally, the dominant frequency of the F-TENG almost remains constant at 30 Hz, showcasing its reliable performance in perceiving vibration. Figure S10 (Supporting Information) depicts that the V_{oc}, Q_{sc} and I_{sc} of the F-TENG rise linearly from 25.1 V, 8.5 nC, 0.6 μA to 58.1 V, 20.6 nC, 1.6 μA as the number of the F-TENG in series increases from 1 to 5. The experimental result not only suggests the possibility of improving the electrical performance using multiple devices but also demonstrates its potential as a energy harvester for harvesting vibration energy.

Due to its outstanding flexibility, F-TENG is able to conform to a variety of irregular surfaces. Herein, the adaptability of the F-TENG is tested on three typical structures (i.e., cylinder, cone and bearing cover) with non-planar surfaces and at fixed

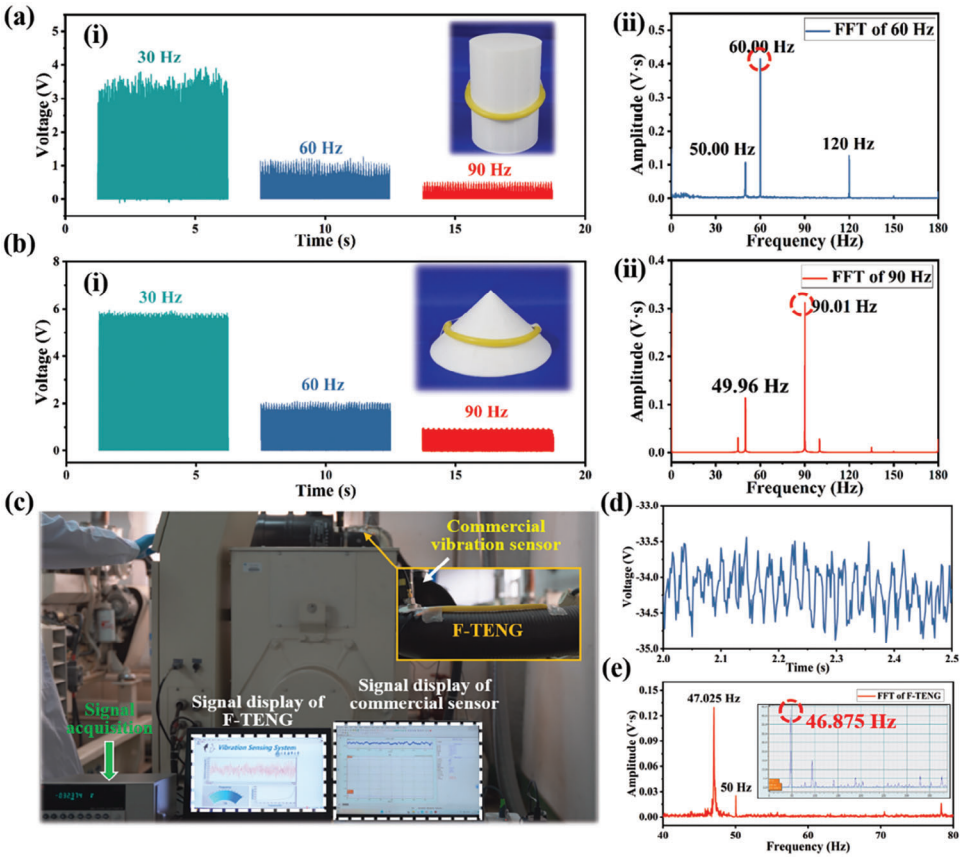

Figure 4. Adaptability test and practical application of the F-TENG. a-i) Generated V_{oc} of the device as attaching on the surface of cylinder at vibration frequencies of 30, 60, and 90 Hz. ii) Corresponding Fourier transform of the original signal at frequency of 60 Hz. b-i) Generated V_{oc} of the F-TENG as attaching on the surface of cone at vibration frequencies of 30, 60, and 90 Hz. ii) Corresponding Fourier transform of the original signal at frequency of 90 Hz. c) Photographic image of F-TENG applied to a real machinery. d) Real-time signal generated by F-TENG for monitoring the real machine. e) Comparison of the Fourier transform by the F-TENG and commercial vibration sensor.

vibration acceleration of 20 m s^{-2} as illustrated in **Figure 4**a,b and Figures S11–S13 (Supporting Information). The V_{oc} of the F-TENG decreases with frequencies increasing from 30 to 60 Hz as mounted on the various structures. Notably, the V_{oc} of the F-TENG as mounted on the cone is larger than those on the cylinder and bearing cover, possibly due to the diverse acceleration vertically acting on the F-TENG. However, the attaching of the device in the arc-shaped curved surface of the bearing cover impedes its radial deformation as exposing to vibration, which leads to a smaller voltage. While it can be seen that the Fourier transform signal of the F-TENG can precisely detect the vibration frequency of the sources with curved surfaces as shown in Figure 4a,b and Figures S11–S13 (Supporting Information).

Then, the F-TENG is affixed to a real diesel engine to evaluate its ability in detecting vibrations in practical mechanical equipment, as depicted in Figure 4c and Movie S1 (Supporting Information). A signal acquisition device and a signal display module are included in the machinery vibration monitoring system. A commercial accelerometer is employed as a reference sensor to assess the ability of the device. As operating the machine, the generated voltage signal is depicted in Figure 4d. Frequency domain analysis reveals that the F-TENG exhibited a primary vibration frequency of 47.025 Hz. And the commercial sensor detected a primary vibration frequency of 46.875 Hz (Figure 4e). The error in detecting the machine vibration is only 0.32%. The demonstration therefore confirms the viability of the designed TENG as a self-powered vibration sensor for practical application.

3.3. Vibration State Recognition by F-TENG Assisted by Deep Learning

Pipeline system plays a crucial role in transporting fluids or gases and maintaining the necessary functions for the operation of the machinery. However, there are still limited methods available for vibration sensing in pipeline systems. On the basis of the capability of precisely perceiving the vibration frequencies, enabled by deep learning, a pipe condition monitoring system is further constructed to distinguish the operational conditions. The typical pipe system commonly consists of machine, pipe, flange, and support (**Figure 5**a), wherein any malfunction may result in the abnormal vibration. As show in Figure 5b, the triboelectric signals acquired by F-TENG are delivered to the conditioning module, and signal acquisition module (The detailed fault conditions can be seen in the inset of Figure S14, Supporting Information). While it is not intuitive and reliable enough to artificially

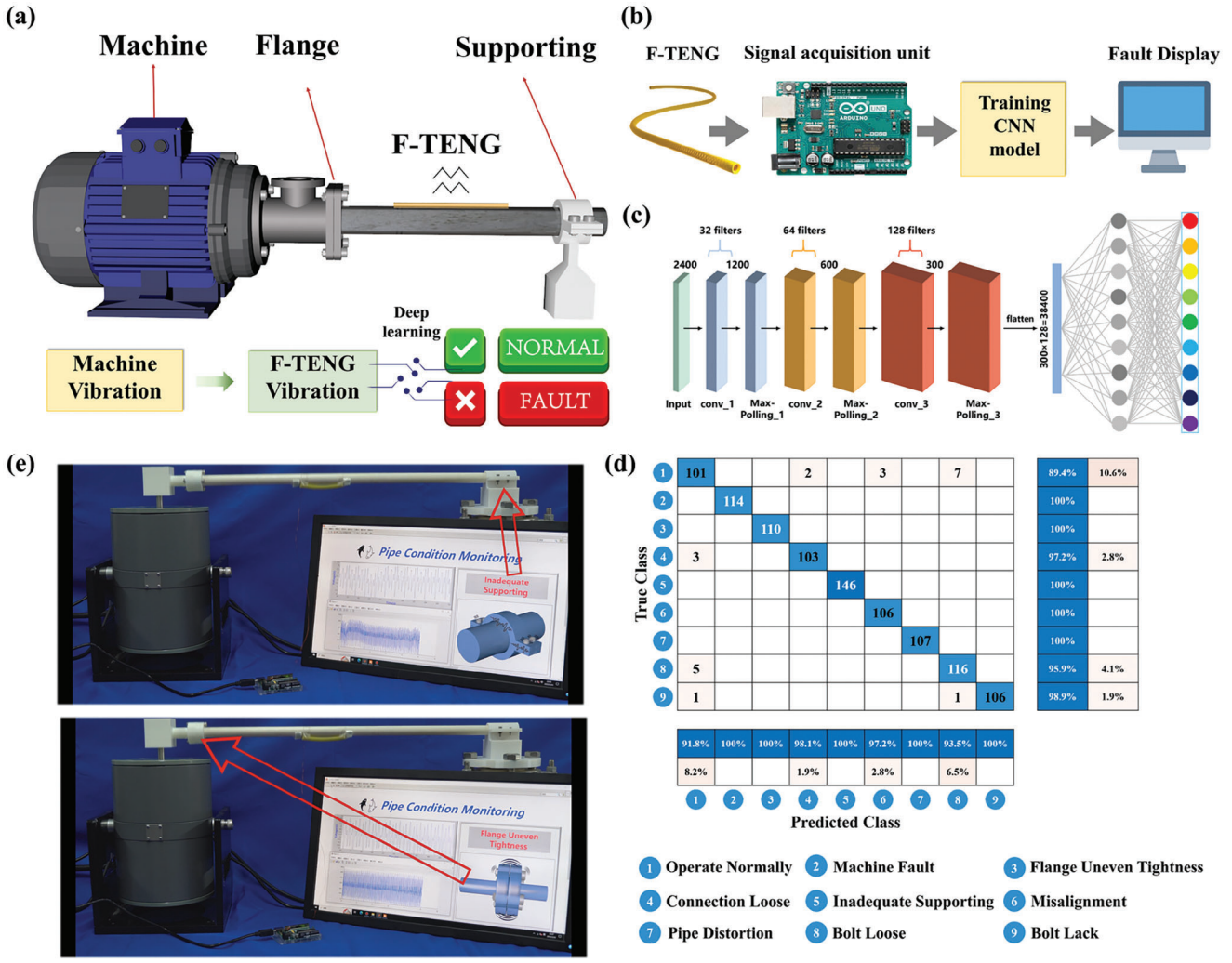

Figure 5. Demonstration of the pipe condition monitoring enabled by deep learning using the F-TENG. a) Design drawing of the pipe condition monitoring system. b) Logical block diagram of F-TENG applied in pipe condition monitoring. c) Detailed structure of CNN training model. d) Confusion matrix for identifying various operation conditions of the pipe system. e) The photograph image of identifying various operating conditions using F-TENG.

recognize the operating conditions (e.g., operate normally, inadequate supporting and bolt loose) of the system just through the time-domain or frequency-domain signals as shown in Figure S14 (Supporting Information). And, deep learning has been widely accepted as a time-efficient approach to recognize the representative yet subtle features from the acquiring signals.[41,42] Subsequently, the signals are trained via Convolutional Neural Network (CNN) model for fault recognition. And fault types can be displayed on the screen. In this work, the signals generated by the F-TENG under operating conditions (operate normally, machine fault, flange uneven tightness, etc,.) are collected as the data set for fault diagnosis. The dataset comprises a total of 2400 samples (≈70% for training and 30% for testing). And CNN model is created in order to exactly distinguish the signals under various conditions as shown in Figure 5c. The confusion matrix reveals that an average recognition accuracy of 97.87% can be obtained after training (Figure 5d). The result demonstrates the potential of deep learning in accurately identifying system faults. Then, the operating conditions of the pipe systems are displayed in real-time on the monitoring screen as indicated in Figure 5e; Movie S2 (Supporting Information).

4. Conclusion

In summary, the first fiber-shaped TENG that can perceive the vibrations has been designed. The device exhibits remarkable capability in responding to the vibration together with the feature of high adaptability and industry-friendly. Besides, this coaxial structure device is also able to perceive the vibration in a broadband frequency range. The experimental results reveal that the optimized F-TENG can perceive the vibration frequency from 10 to 100 Hz. More interestingly, the device also exhibits its ability in perceiving the movement with frequencies as low as 0.1 Hz. Comparing to the previous TENG-based vibration sensors, the flexible and compact design enables the device to conform to various curved structures, thereby reducing the installation difficulty. The practical applications of the F-TENG in a real diesel engine has demonstrated the feasibility in detecting

the vibration. The detection error is only 0.32% comparing to commercial vibration sensors. Finally, the F-TENG is successfully utilized in monitoring the working conditions of the pipe system assisting by deep learning, and the fault recognition accuracy reaches 97.87%. Considering its nature of self-powered and industry-friendly, it is believed that the newly designed device can meet the distributed monitoring requirement in Industry 4.0.

5. Experimental Section

Electrical Measurements: The element distribution of conductive yarn was characterized by the energy dispersive spectroscopy (Oxford X-MaxN). A Field Emission Microscopy (HiTACHI S-4800) was utilized to observe the surface pattern of the conductive yarn. The vibration sources were simulated through an electrodynamic shaker (JZK-20). In order to calibrate the vibration acceleration of the shaker, a commercial accelerometer (BWT61CL) was utilized. Through an amplifier (YE5852), the vibration acceleration and frequency could be precisely adjusted. The low-frequency vibration was simulated through a linear motor (Linmot E1100). And a electrometer (Keithley 6514) was utilized to measure the open-circuit voltage, short-circuit current, and transferred charge of the F-TENG. In the demonstration of distinguishing the various faults of the pipe system, an Arduino Uno was applied to acquire the signal outputs of the F-TENG.

Supporting Information

Supporting Information is available from the Wiley Online Library or from the author.

Acknowledgements

C.Z., T.D., and B.G. contributed equally to this work. The work was supported by the National Natural Science Foundation of China (Grant Nos. 52101345, 52101400), the Scientific Research Fund of the Educational Department of Liaoning Province (Grant No. LJKZ0055), the Dalian Outstanding Young Scientific and Technological Talents Project (2021RJ11), the Open Fund of National Center for International Research of Subsea Engineering Technology and Equipment (No. 3132023354).

Conflict of Interest

The authors declare no conflict of interest.

Data Availability Statement

The data that support the findings of this study are available from the corresponding author upon reasonable request.

Keywords

fiber-shaped sensors, self-powered sensors, triboelectric nanogenerators, vibration sensors

Received: September 3, 2023
Revised: October 18, 2023
Published online:

[1] K. S. Kiangala, Z. Wang, *Int. J. Adv. Manuf. Technol.* **2018**, *97*, 3251.
[2] J. Dalzochio, R. Kunst, E. Pignaton, A. Binotto, S. Sanyal, J. Favilla, J. Barbosa, *Comput. Ind.* **2020**, *123*, 103298.
[3] M. Compare, P. Baraldi, E. Zio, *IEEE Internet Things J.* **2020**, *7*, 4585.
[4] M. Javaid, A. Haleem, R. P. Singh, S. Rab, R. Suman, *Sens. Int.* **2021**, *2*, 100110.
[5] J.-D. Son, G. Niu, B.-S. Yang, D.-H. Hwang, D.-S. Kang, *Expert Syst. Appl.* **2009**, *36*, 11981.
[6] Q. Zhang, K. Barri, S. R. Kari, Z. L. Wang, A. H. Alavi, *Adv. Funct. Mater.* **2021**, *31*, 23.
[7] P. M. Harikrishnan, V. P. Gopi, *IEEE Sens. J.* **2017**, *17*, 5192.
[8] E. Caetano, S. Silva, J. Bateira, *Exp. Tech.* **2011**, *35*, 74.
[9] J. Mu, H. He, J. Mu, J. He, J. Song, X. Han, C. Feng, J. Zou, J. Yu, X. Chou, *Sci. China Technol. Sci.* **2022**, *65*, 1545.
[10] T. Du, X. Zuo, F. Dong, S. Li, A. E. Mtui, Y. Zou, P. Zhang, J. Zhao, Y. Zhang, P. Sun, M. Xu, *Micromachines* **2021**, *12*, 218.
[11] K. Liu, Z. Sun, J. Jiang, P. Ma, S. Wang, L. Weng, Z. Xu, T. Liu, *IEEE Access* **2019**, *7*, 105609.
[12] C. Xu, J. Guan, M. Bao, J. Lu, W. Ye, *Opt. Eng.* **2018**, *57*, 016103.
[13] T. Li, C. Shi, Y. Tan, R. Li, Z. Zhou, H. Ren, *IEEE Sens. J.* **2017**, *17*, 1021.
[14] Y. Wang, Z. Qian, C. Zhao, Y. Wang, K. Jiang, J. Wang, Z. Meng, F. Li, C. Zhu, P. Chen, H. Wang, M. Xu, *Adv. Mater. Technol.* **2023**, *8*, 2201245.
[15] E. Sazonov, Haodong Li, D. Curry, P. Pillay, *IEEE Sens. J.* **2009**, *9*, 1422.
[16] Z. L. Wang, *Nano Today* **2010**, *5*, 512.
[17] X. Chen, L. Luo, Z. Zeng, J. Jiao, M. Shehzad, G. Yuan, H. Luo, Y. Wang, *J. Mater.* **2020**, *6*, 643.
[18] B. Zhang, L. Zhang, W. Deng, L. Jin, F. Chun, H. Pan, B. Gu, H. Zhang, Z. Lv, W. Yang, Z. L. Wang, *ACS Nano* **2017**, *11*, 7440.
[19] B. Zhang, Z. Wu, Z. Lin, H. Guo, F. Chun, W. Yang, Z. L. Wang, *Mater. Today* **2021**, *43*, 37.
[20] X. Chen, Q. Zeng, J. Shao, S. Li, X. Li, H. Tian, G. Liu, B. Nie, Y. Luo, *ACS Appl. Mater. Interfaces* **2021**, *13*, 34637.
[21] R. Salazar, M. Serrano, A. Abdelkefi, *Appl. Energy* **2020**, *270*, 115161.
[22] Z. Lin, C. Sun, G. Zhang, E. Fan, Z. Zhou, Z. Shen, J. Yang, M. Liu, Y. Xia, S. Si, J. Yang, *Nano Res.* **2022**, *15*, 7484.
[23] S. Liu, Y. Shan, Y. Hong, Y. Jin, W. Lin, Z. Zhang, X. Xu, Z. Wang, Z. Yang, *Adv. Sci.* **2022**, *9*, 2106030.
[24] C. Zhao, D. Liu, Y. Wang, Z. Hu, Q. Zhang, Z. Zhang, H. Wang, T. Du, Y. Zou, H. Yuan, X. Pan, J. Mi, M. Xu, *Nano Energy* **2022**, *94*, 106926.
[25] T. Du, F. Dong, R. Xu, Y. Zou, H. Wang, X. Jiang, Z. Xi, H. Yuan, Y. Zhang, P. Sun, M. Xu, *Adv. Mater. Technol.* **2022**, *7*, 2200003.
[26] Y. Wang, Z. Hu, J. Wang, X. Liu, Q. Shi, Y. Wang, L. Qiao, Y. Li, H. Yang, J. Liu, L. Zhou, Z. Yang, C. Lee, M. Xu, *ACS Appl. Mater. Interfaces* **2022**, *14*, 24832.
[27] Y. Wang, D. Liu, Z. Hu, T. Chen, Z. Zhang, H. Wang, T. Du, S. L. Zhang, Z. Zhao, T. Zhou, M. Xu, *Adv. Mater. Technol.* **2021**, *6*, 2001270.
[28] P. Xu, J. Liu, X. Liu, X. Wang, J. Zheng, S. Wang, T. Chen, H. Wang, C. Wang, X. Fu, G. Xie, J. Tao, M. Xu, *npj Flexible Electron.* **2022**, *6*, 25.
[29] X. Xiao, X. Zhang, S. Wang, H. Ouyang, P. Chen, L. Song, H. Yuan, Y. Ji, P. Wang, Z. Li, M. Xu, Z. L. Wang, *Adv. Energy Mater.* **2019**, *9*, 1902460.
[30] S. Li, D. Liu, Z. Zhao, L. Zhou, X. Yin, X. Li, Y. Gao, C. Zhang, Q. Zhang, J. Wang, Z. L. Wang, *ACS Nano* **2020**, *14*, 2475.
[31] Y. Chen, Y.-C. Wang, Y. Zhang, H. Zou, Z. Lin, G. Zhang, C. Zou, Z. L. Wang, *Adv. Energy Mater.* **2018**, *8*, 1802159.
[32] H. Luo, Y. Lu, Y. Xu, G. Yang, S. Cui, D. Han, Q. Zhou, X. Ouyang, H. Yang, T. Cheng, K. Xu, *Nano Energy* **2022**, *103*, 107803.
[33] J. Han, C. Xu, J. Zhang, N. Xu, Y. Xiong, X. Cao, Y. Liang, L. Zheng, J. Sun, J. Zhai, Q. Sun, Z. L. Wang, *ACS Nano* **2021**, *15*, 1597.
[34] X. He, Y. Zi, H. Guo, H. Zheng, Y. Xi, C. Wu, J. Wang, W. Zhang, C. Lu, Z. L. Wang, *Adv. Funct. Mater.* **2017**, *27*, 1604378.
[35] X. Guan, B. Xu, J. Huang, T. Jing, Y. Gao, *Chem. Eng. J.* **2022**, *427*, 131698.

[36] X. Yu, J. Pan, J. Zhang, H. Sun, S. He, L. Qiu, H. Lou, X. Sun, H. Peng, *J. Mater. Chem. A* **2017**, *5*, 6032.
[37] M. He, Y. Wang, S. Wang, S. Luo, *Carbon* **2020**, *168*, 308.
[38] I. Golebiowska, K. Peszynski, *EPJ Web Conf.* **2018**, *180*, 02031.
[39] L. Lu, Y.-F. Duan, B. F. Spencer, X. Lu, Y. Zhou, *Struct. Control Health Monit.* **2017**, *24*, e1986.
[40] F.-R. Fan, L. Lin, G. Zhu, W. Wu, R. Zhang, Z. L. Wang, *Nano Lett.* **2012**, *12*, 3109.
[41] L. Wen, X. Li, L. Gao, Y. Zhang, *IEEE Trans. Ind. Electron.* **2018**, *65*, 5990.
[42] F. Jia, Y. Lei, L. Guo, J. Lin, S. Xing, *Neurocomputing* **2018**, *272*, 619.